

The vulnerability of buildings to a large-scale debris flow and outburst flood hazard **cascade** that occurred on 30 August 2020 in Ganluo, Southwest China

Li Wei ¹, Kaiheng Hu¹, Shuang Liu¹, Lan Ning ^{1,2}, Xiaopeng Zhang^{1,2}, Qiyuan Zhang^{1,2}, Md Abdur Rahim^{1,2,3}

¹ Key Laboratory of Mountain Hazards and Earth Surface Processes, Institute of Mountain Hazards and Environment, Chinese Academy of Sciences, Chengdu 610041, China

²University of Chinese Academy of Sciences, Beijing 100149, China.

³Department of Disaster Resilience and Engineering, Patuakhali Science and Technology University, Dumki, Patuakhali-8602, Bangladesh

Abstract: In mountainous areas, damage caused by debris flows is often aggravated by subsequent dam-burst floods within the main river confluence zone. On 30 August 2020, a catastrophic disaster chain occurred at the confluence of the Heixiluo Gully and Niri River in Ganluo County, Southwest China, that consisted of a debris flow, the formation of a barrier lake and subsequent dam **break** that flooded the community. This study **presents** a comprehensive analysis of **the characteristics of two hazards and the resulting** damage to buildings from the **cascading hazards**. The peak discharge of the debris flow in the gully mouth reached **1,871** m³/s, and the change in the main river channel resulting from the dam-burst flood, which had a peak discharge of **2,737** m³/s, resulted in a fourfold increase in the extent of flood inundation compared to an ordinary flood. Three hazard zones were established based on the building damage patterns: (I) primary debris flow burial; (II) secondary dam-burst flood inundation and (III) sequential debris flow burial and dam-burst inundation. Vulnerability curves were developed for Zone (II) and Zone (III) using impact pressures and inundation depths, and a vulnerability assessment chart is presented that contains the three damage categories. This research addresses a gap in the vulnerability assessments of debris flow hazard cascades and can support future disaster mitigation within confluence areas.

Keywords: Multi-hazard risk, Debris flow, Dam-burst flood, Building damage, Vulnerability analysis.

1 Introduction

In mountainous areas, debris flows frequently block rivers and form temporary dammed lakes. The subsequent breach of these dammed lakes can result in a vast flash flood (Yan et al., 2020). The hazard **cascade** consisting of debris flows and subsequent dam-burst floods usually **devastate** residential buildings in confluence zones. For instance, a large-scale debris flow occurred in the Wenjia Gully in Sichuan Province, Southwest China, on 13 August 2010 and completely blocked the Mianyuan River, which formed a dammed lake 1,650 m long, 420 m wide, and 12 m deep. Then,

35 the dammed lake breached and caused 7 fatalities and extensive damage to 479 houses (Yu et al.,
36 2013).

37 Multi-hazard analyses that incorporate potential hazard interactions have gained significant
38 attention in recent years (Liu et al., 2015; Gallina et al., 2016; Tilloy et al., 2019; Luo et al., 2023).
39 However, vulnerability assessments in risk analysis rarely consider the effects of hazard
40 interactions (Luo et al., 2023). Argyroudis et al. (2019) introduced a new methodology for
41 evaluating the vulnerability of transport infrastructure to multiple hazards. This approach is
42 comprised of six steps and includes numerical and fragility models. Progress has been made in
43 assessing the risk of buildings exposed to multiple hazards by considering the interaction between
44 an earthquake and other hazards, such as dam breaks, flash floods, and tsunamis. Korswagen et al.
45 (2019) proposed a methodology for assessing structural damage resulting from coupled hazards
46 and used it to assess the vulnerability of a masonry building subjected to an earthquake and an
47 earthquake-triggered dam break. Furthermore, Park et al. (2012) developed collapse fragility curves
48 for earthquake and tsunami effects using a numerical model. Gautama and Dong (2018) outlined
49 the vulnerability of vernacular stone masonry buildings to the flash floods that occurred after the
50 Gorkha earthquake. Residential buildings in Nepal were found to have up to 300% damage
51 resulting from the combined earthquake and subsequent flash flood. Petrone et al. (2020) simulated
52 the response of reinforced concrete frames to earthquake and tsunami inundation, yielding fragility
53 curves that showed a median decrease of less than 15% in terms of tsunami resistance when exposed
54 to cascading hazards as compared to tsunami-only fragility functions.

55 The evaluation and mitigation of the multiple risks posed by debris flows and dam-burst floods
56 in a confluence zone require a multi-risk analysis that considers hazard interactions and their
57 cumulative effects on building vulnerability. Most studies on debris flow and dam-burst floods
58 mainly focus on numerical simulations and the evolving processes of hazard cascades (Cutter, 2018;
59 Nin et al., 2022; Chen et al., 2022), but studies on the vulnerability of building to hazard cascades
60 are scarce. The vulnerability of buildings to the cumulative impact of debris flow and flash flood
61 may differ from the sum or sequence of vulnerability resulting from a single debris flow or flash
62 flood (Kappes et al., 2012). The effect that simultaneous hazards have on building vulnerability
63 remains inadequately addressed, with only a few studies available (Kappes et al., 2012). Luo et al.
64 (2020) proposed a framework for developing physics-based vulnerability models for buildings
65 exposed to multiple surges of debris flows. Cumulative damage effects resulting from sequentially
66 occurring debris flows were quantified by assessing the physical damage from primary debris flows.
67 However, this approach may not apply directly to the debris flow-dam-burst flood hazard cascade.

68 Field investigations have shown that the pattern of damage to buildings in the confluence area
69 of debris flow and flood is not consistent with those from the debris fan or on the floodplain. **Our**
70 **field investigations have revealed that the pattern of damage to buildings in the confluence area of**
71 **debris flow and flood is distinct from those observed in areas affected by debris flow alone or by**
72 **flood alone.** Debris flow usually causes devastating damage to settlements on the fan, and the
73 subsequent dam-burst flood significantly increases the damage (Xu et al., 2014; Yu et al., 2013).
74 The risk amplification and cumulative effect on building vulnerability resulting from successive
75 debris flows and dam-burst floods are not entirely clear. Therefore, in-depth analysis is essential
76 for assessing the risks posed by the debris flow hazard **cascade** to develop a successful emergency
77 management plan.

78 On August 30, 2020, a catastrophic debris flow and dam-burst flood occurred in the Niri River,
79 Ganluo County, Sichuan Province, Southwest China. This study aims to comprehensively analyze
80 the damage to buildings caused by the Heixiluo debris flow-dam-burst flood disaster chain. Firstly,
81 we calculated the dynamic characteristics of the debris flow and outbreak flood damage. We then
82 systematically investigated and summarized the building damage characteristics and analyzed and
83 compared the vulnerability of buildings considering different damage patterns. Finally, we discuss
84 how the damage was amplified by the chain and offer suggestions for hazard mitigation.

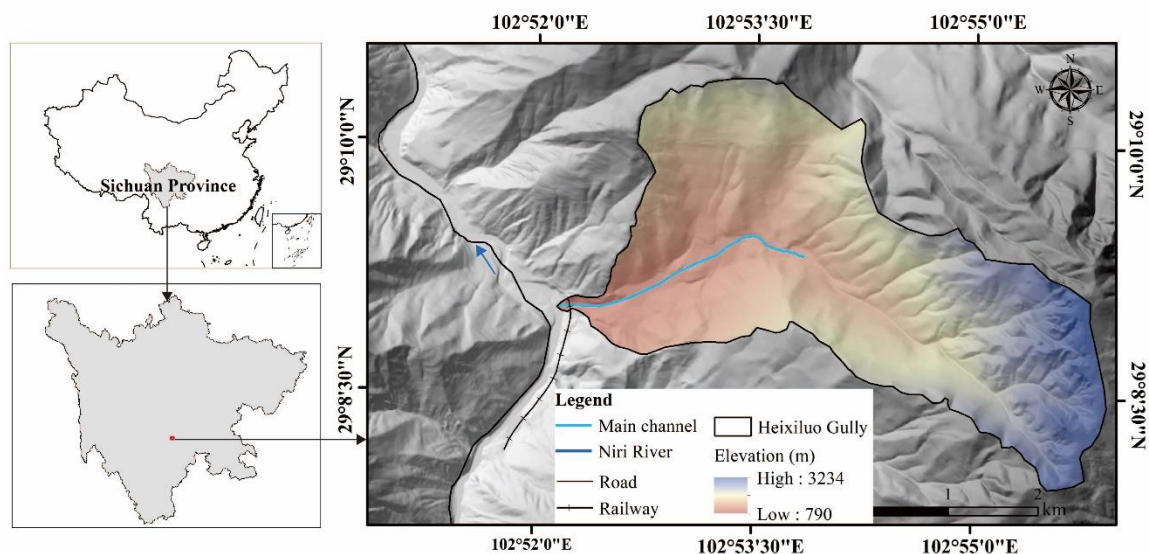
85 **2 Study area**

86 The study area is located in Ganluo County, Sichuan Province, Southwest China, which
87 includes the Heixiluo Gully and the confluence area along the Niri River. Ganluo County lies north
88 of the Liangshan Yi Autonomous Prefecture, occupying the alpine canyon zone in the transitional
89 region between the western margin of the Sichuan Basin and the Qinghai-Tibet Plateau (Fig. 1).
90 The geographic boundaries of the study area span from 102°27' to 103°01' east longitude and from
91 28°38' to 29°18' north latitude. Ganluo County covers a total area of 2150.97 km² and had a
92 permanent population of 205,991 at the end of 2020.

93 Ganluo County consists of an erosional tectonic landform that is defined by two primary
94 structures, namely Sichuan-Yunnan north-south structure and the Qinghai-Tibet Yunnan zeta-type
95 structure. The mountain and river systems flow from south to north due to the folds, uplift, and
96 fractures of the Hengduan Mountains and the strong disruptive effect that widely distributed rivers,
97 undulating hills, ravines, and cliffs have on the study area. The valleys, which are characterized by
98 a V-shaped cross-section, have considerable depths that typically exceed 1000 meters.

99 Folds are ubiquitous in the study area, and the N-S trending Teke fault, Suxiong anticline, and
100 Maanshan anticline are excellent examples of these typical geological structures. These faults were
101 last active during the early and middle Pleistocene and there is no discernible evidence that they

102 were active during the late Quaternary period. The exposed strata in the study area are primarily
 103 comprised of Quaternary strata (Q), Presinian Ebian Group (Pteb), and Lower Sinian Suxiong
 104 Group (Zas). The upstream area is mainly occupied by sandstone, whereas rhyolite and tuff
 105 dominate the main part of the catchment, with slate occupying the left downstream area. The study
 106 area is situated in a seismically active region. The peak ground acceleration in the study area is 0.15
 107 g, and the peak period of the seismic response spectrum is 0.45 s. Between 1327 and 1975, nearly
 108 147 $M_s \geq 2.5$ earthquakes were recorded, including 15 $M_s \geq 5.0$ earthquakes with the highest
 109 magnitude of 7.5.



110
 111 **Figure 1** Location of the study area including the Heixiluo Gully and Niri River.

112 The Niri River is a first-order tributary of the middle reaches of the Dadu River and flows from
 113 south to north and over an elevation range of 1,800-2,200 a.s.l. for most of the areas. The highest
 114 elevation in the river basin is 4,700 m a.s.l., and the lowest elevation is 1170 m a.s.l. The study area
 115 has a subtropical monsoon climate. **The average annual temperature is 16.2° and the average**
 116 **annual rainfall is 949 mm.** The precipitation is distributed unevenly throughout the year. The
 117 rainfall is concentrated from April to October, with an average rainfall of 901.9 mm, accounting
 118 for 93.14% of the average annual rainfall. The precipitation varies significantly with elevation, with
 119 an annual precipitation of 968 mm, and the maximum hourly rainfall and ten-minute rainfall
 120 recorded are 40.3 mm and 14.8 mm, respectively.

121 The Heixiluo Gully is located on the right bank of the Niri River in Suxiong town, Ganluo County
 122 (Fig. 1). The coordinates of the gully mouth are 29° 09' 47" N and 102° 52' 53" E and the
 123 gully extends from the east to the west. The gully covers an area of 13.36 km² and is situated at a
 124 moderate elevation on the mountainous landform. The catchment elevation ranges from 3,220 m

125 a.s.l. to 760 m a.s.l., with a relative height of 2,460 m. The main channel of the gully stretches for
126 6.93 km, with an average gradient of 0.355. The average slopes for areas above and below 1,990
127 m are approximately 0.6 and 0.256, respectively.

128 The field investigation indicates that debris flow initiated in the area above an elevation of
129 1,990 m a.s.l. The gradient of the channel in this area is steep, with an average value of 0.6. The
130 transportation zone is mainly located between 820 m a.s.l. and 1,990 m a.s.l. in elevation and
131 occupies an area of 5.96 km². The length of the main gully is 4.65 km, and the average gradient of
132 the main gully is 0.252. Two platforms were distributed at altitudes of 1,160 m a.s.l. and 1,030 m
133 a.s.l. and divided the main channel of the transportation zone into three parts. A narrow channel
134 developed between the platform and the deposition fan at 1023 m a.s.l. The length and gradient of
135 the channel are approximately 670 m and 0.243, respectively.

136 **3 Data and methods**

137 We conducted field investigations on the debris flow-flash floods that occurred on 31 August and
138 3 December 2020. The field survey mainly focused on the main transportation and deposition zones.
139 Interviews, measurements, and aerial photography were conducted to investigate the formation and
140 disaster mechanisms. The geomorphic settings of the Heixiluo Gully and adjacent Niri River were
141 carefully measured and analyzed, including the channel width, deposition and erosion height,
142 channel slope, and particle size distributions. The damage to buildings was also investigated by
143 comparing the drone photos taken before and after the disaster.

144 **3.1 Data collection**

145 The Digital Elevation Models (DEMs) collected before and after the event were used for hazard
146 cascade analysis. The pre-event DEM was converted from a 1:10000 topographic contour map
147 provided by the Sichuan Bureau of Surveying, Mapping, and Geoinformation which had a spatial
148 resolution of 10 m. The post-event DEM of the study area was produced by synthesizing high-
149 resolution aerial images captured by a Dajiang unmanned aerial vehicle (UAV) on 3 December
150 2020. To calibrate the post-event terrain, 10 image control points that were not affected by the
151 disaster were selected, and their elevation values were sampled from the pre-DEM and assigned as
152 input conditions. The mean RMS error of georeferencing of the post-event DEM was within the
153 usable range with a value of 0.1 m.

154 **3.2 Methodology**

155 The dynamic parameters of the debris flow and discharge of the dam-burst flood were calculated
156 by the formulas presented in Table 1.

Table 1 Models used in parameter calculation for this study

Category of Calculation	Applied formula	Description parameters
Debris flow density (Hu et al., 2019)	$\gamma_c = -1320x^7 - 513x^6 + 891x^5 - 55x^4 + 34.6x^3 - 67x^2 + 12.5x + 1.55$	x is the clay content in the debris flow sample. The average clay content in particles less than 0.005 mm in size accounts for 2.55%.
Debris flow peak discharge and velocity (Kang, 1987; Yang, 1985)	$Q = \frac{1}{n_c} AR^{\frac{2}{3}} J^{\frac{1}{2}}$ $n_c = \frac{1}{18.5H^{-0.42}}$ $U = \frac{Q}{A}$	A is the cross-sectional area, R is the hydraulic radius, J is the channel bed gradient, and n_c is the roughness coefficient for viscous debris flow. The method for calculating n_c was deduced from analysis of viscous debris flows in Huoshao gully in China.
Dam-burst flood discharge	$Q = \frac{1}{n} AR^{\frac{2}{3}} J^{\frac{1}{2}}$	A is the cross-sectional area, R_n is the hydraulic radius, J is the channel bed gradient, and n is the Manning roughness coefficient. The values of A, R_n , and J were directly measured by the field investigation.

158 The debris flow depth and velocity were obtained by numerical simulations performed using
 159 FLO-2D software (O'Brien, 1986). FLO-2D is a simple volume conservation model that can
 160 simulate non-Newtonian flows and has been employed successfully to simulate debris flows by
 161 many researchers. The input parameters in FLO-2D include Manning's n coefficient, laminar flow
 162 resistance parameter k , and empirical coefficients α and β . The estimated peak discharge at the
 163 gully mouth using Kang's equation (1987) was applied in the simulation. The data used in the debris
 164 flow simulation are presented in Table 2.

Table 2 Data used in the flood simulation

Discharge	Manning's n-value	Viscosity coefficient		Yield stress coefficient		Laminar flow resistance coefficient k
		α_1	β_1	α_2	β_2	
Estimated by Kang's equation (1987) at the gully mouth	0.4 (river channel), 0.2 (building in the floodplain), 0.03 (cultivated land)	3.22	5.8293	0.0612	15.877	2,285

166 Dam-burst flood hydraulics were simulated by HEC-RAS 5.0.7 (Hydrologic Engineering Center,
 167 2016) using the post-event DEM. The computation procedure employed a one-dimensional steady
 168 flow simulation and assumed a subcritical flow regime. The boundary conditions are established at
 169 all the ends of the river nodes by entering the normal depth value. The initial conditions were set
 170 using the corresponding discharge of the dam-burst flood estimated at a typical river section using
 171 Manning's equation. Manning's n coefficient, expansion, and contraction coefficients account for
 172 flow energy losses in HEC-RAS.

173 The upstream inflow flood hydraulics were also calculated by HEC-RAS 5.0.7. The flood
 174 discharge was obtained from upstream hydrological observation stations located approximately 15
 175 km from Heixiluo Gully. Due to the difficulty of acquiring terrain data for the initial stage of the

176 dam break, it was assumed that the peak discharge of the dam-burst flood formed the post-event
 177 terrain, which was adopted to simulate the dam-burst flood. To analyze the impact of debris flows
 178 on river dynamics, we also simulated an ordinary flood unaffected by debris flows using the pre-
 179 event DEM. The Manning's n values for the river channel and floodplain were 0.4 and 0.2,
 180 respectively. These values are the suggested values for main channels that are clean and winding,
 181 have some pools and shoals, some weeds and stones, and have flood plains for cultivated areas but
 182 are free of crops (Hydrologic Engineering Center, 2016). The data applied to the flood calculations
 183 are presented in Table 3.

184 **Table 3** Data used in the flood simulation

Flood processing	Data	Data source	Manning's n -value	Expansion and contraction coefficients
Debris flow dam-burst flood	Topography	Post-event DEM of the river channel	0.5 (river channel and floodplain)	0.1 (expansion coefficient) 0.3 (contraction coefficient)
	Discharge	Estimated by Manning's equation in a typical section		
Flood not affected by debris flow	Topography	Pre-event DEM of the river channel	0.4 (river channel), 0.2 (floodplain)	
	Discharge	Record in the Yanrun Hydrometric station (located upstream 23 km from Heixiluo Gully)		

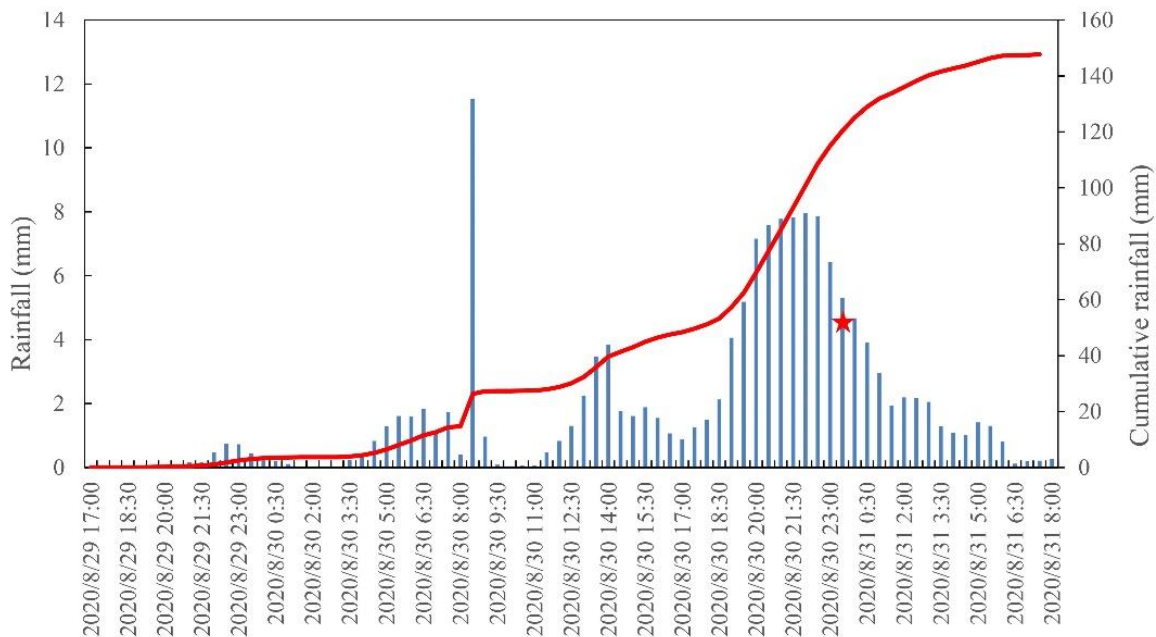
185 A vulnerability curve was developed to describe the relationship between the hazard intensity
 186 and the degree of damage to the buildings. Following the classification of the damage degrees
 187 proposed by Hu et al. (2012), the degree of damage to buildings caused by multi-hazards was
 188 determined through a comprehensive analysis of photographs taken on site and aerial images
 189 collected over the disaster scene. Hazard intensity parameters were applied, such as flow depth and
 190 average total impact pressure, with average total impact pressure calculated as $P = \rho v^2 +$
 191 $0.5\rho gh$ (Zanchetta et al., 2014) where P is the average total impact pressure, ρ is the flow density,
 192 v is the velocity, and h is the flow depth. The deposition depth of the debris flow was obtained by
 193 field investigation, while the velocity was calculated using the method outlined in Table 1. The
 194 maximum flow depth and velocity of the flood were extracted from the HEC-RAS model. A
 195 nonlinear regression analysis was conducted using a logarithmic form expression to relate the
 196 vulnerability to the intensity parameters of the hazard.

197 **4 Results**

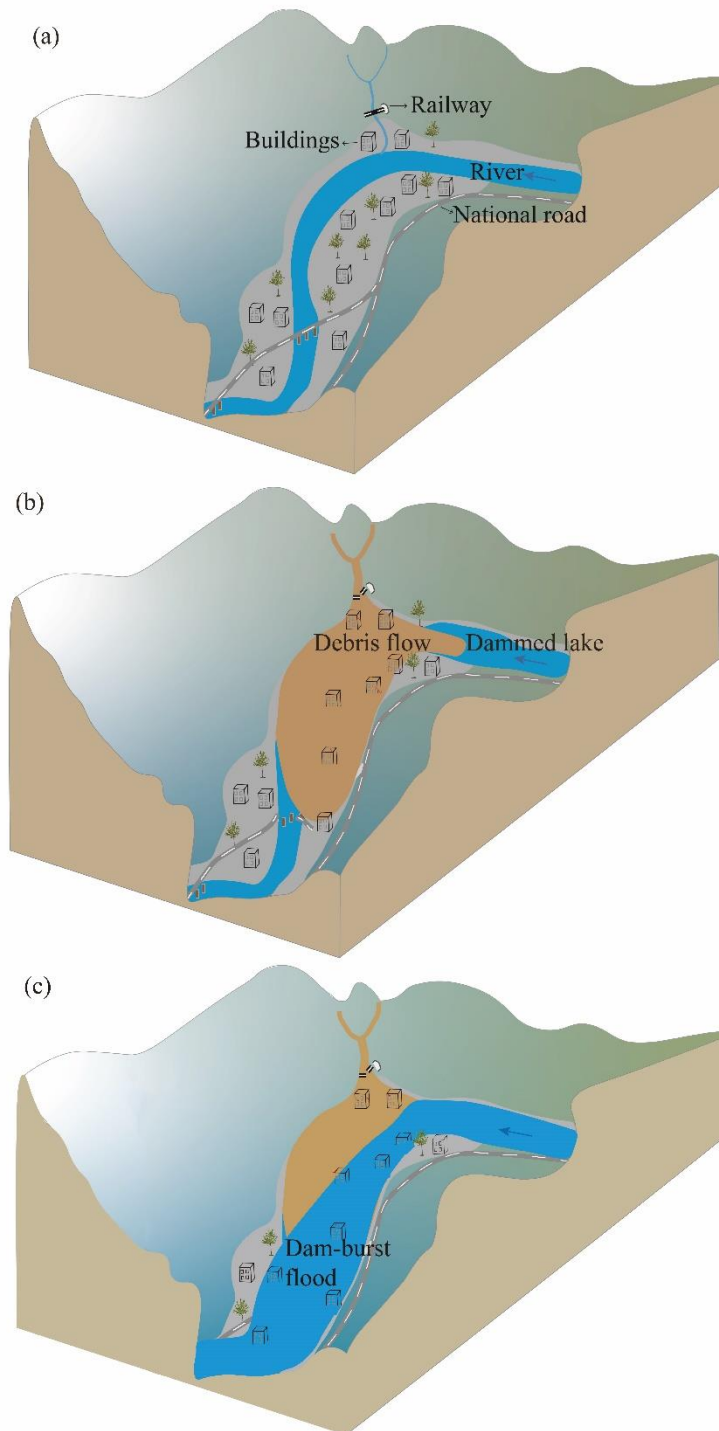
198 **4.1 Hazard cascade**

199 The debris flow was triggered by a once in a century short-term heavy rainfall event. According
200 to the precipitation data from two automated stations located 10 km away, the 24-hour cumulative
201 rainfall from 8:00 on 30 August was approximately 82.8 mm. The rainfall data extracted from the
202 Global Precipitation Measurement (GPM) rainfall product in the Heixiluo Gully showed that the
203 rainfall started on 29 August at 22:00 and lasted until 6:00 on 31 August and delivered a total of
204 147.2 mm of rain. The hourly rainfall increased to 5.18 mm at 19:30 on 30 August, which triggered
205 the debris flow due to the approximately accumulated 61.4 mm of rainfall. The debris flow lasted
206 approximately 40 minutes, and the rainfall intensity reached 6.63 mm/h (Fig. 2). Heavy rainfall
207 caused flooding in the Yanrun Hydrometric station (located 15 km upstream from the study area),
208 resulting in a peak discharge of 893 m³/s (He et al., 2020), which was nearly nine times the **average**
209 **discharge**.

210 The debris flows transported approximately 1,050,000 m³ of material to the Niri River, forming
211 a temporary debris dam that breached after approximately 40 minutes, resulting in a massive flash
212 flood. The debris flow-flash flood event caused significant damages, including the destruction of
213 108 buildings, the Chengdu-Kunming railway bridge near the gully mouth, 1.2 km along national
214 road G245, and 5 highway bridges along the main river (Fig. 3).



215 **Figure 2** Hourly and cumulative rainfall on 29, 30, and 31 August 2020 extracted from the Global
216 Precipitation Measurement (GPM) rainfall product.
217



218

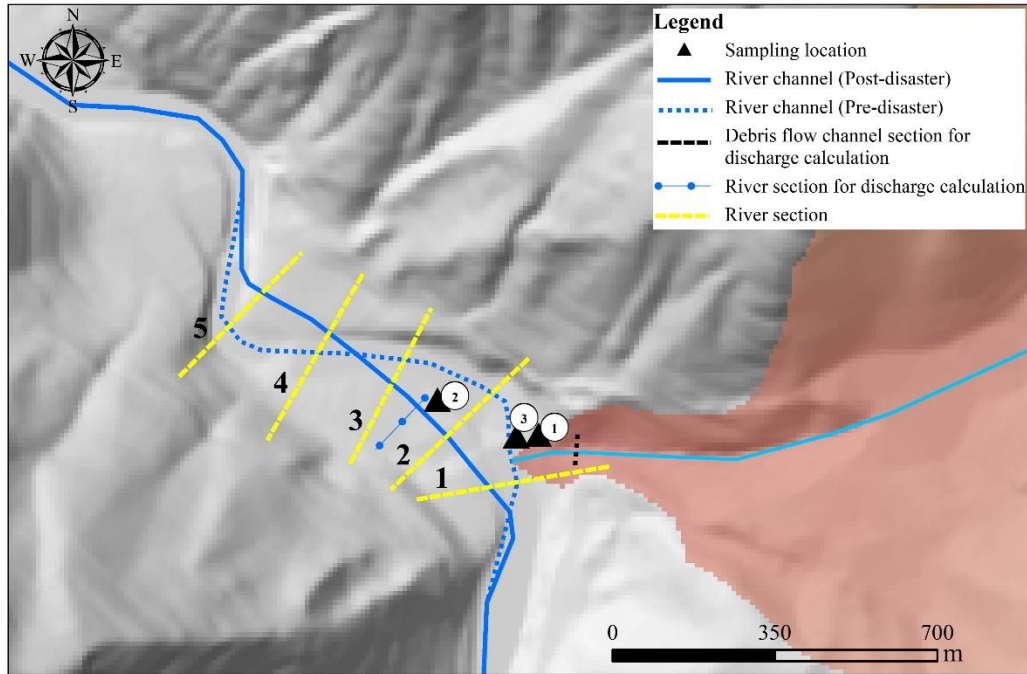
219 **Figure 3** Illustration of the hazard cascade process: (a) the normal flow of river flow before the occurrence

220 of debris flow; (b) debris flow blocks the river, creating a dammed lake that destroys the railway, roads, and

221 buildings; (c) the dammed lake bursts, causing a flood that damaged and the road and buildings

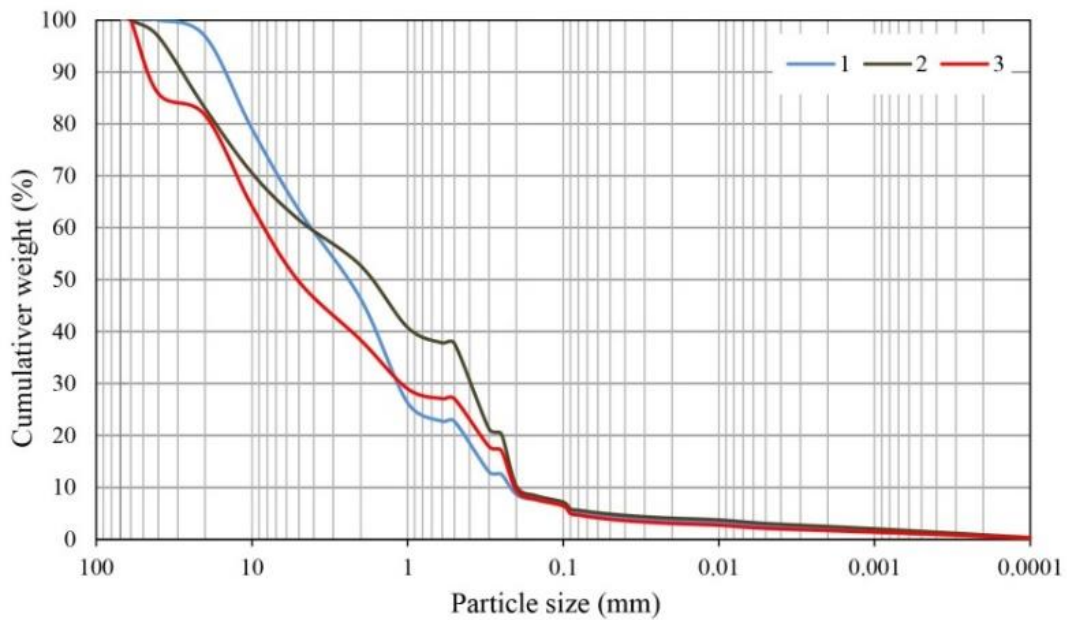
222 **4.2 Dynamic characteristics of the debris flow**

223 Samples of debris particles smaller than 10 cm were taken from three locations (see Fig. 4). The
224 particle size distribution of the debris flow samples is presented in Fig. 5. The calculated bulk
225 density of the debris flow is 1.825 g/cm³, which indicates a viscous debris flow (Kang et al., 2004).



226

227 **Figure 4** Distribution of river and debris flow channel sections and debris flow sampling locations.

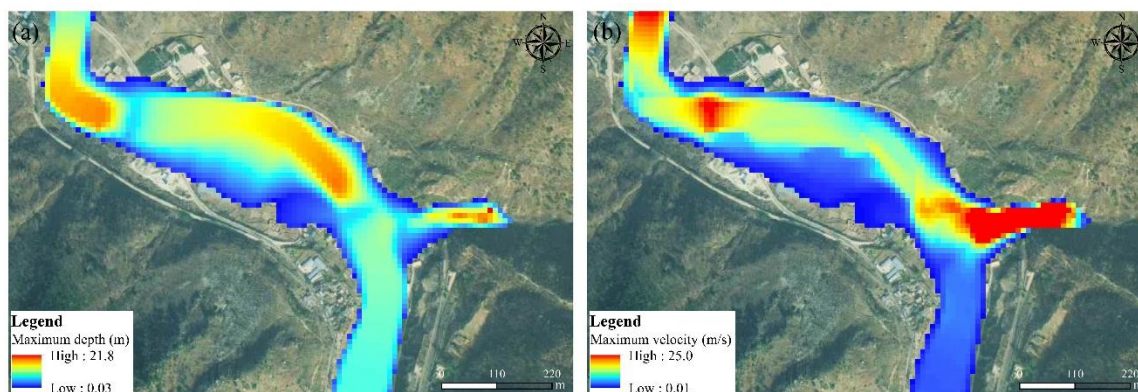


228

229 **Figure 5** Particle size distribution of debris flow samples.

230 The debris flow destroyed the Chengdu-Kunming railway bridge situated at the gully mouth and
231 had a flow depth of approximately 4.7 m and a section area of approximately 188 m². The estimated
232 peak discharge at the gully mouth using Kang's equation (1987) was 1871 m³/s, which resulted in
233 a high impact pressure of 223 kPa.

234 The temporal distributions of the maximum depth and velocity of the debris flow are presented
235 in Fig. 6. Majority of buildings close to the river channel and debris flow channel were buried by
236 the debris flow. The debris flow lasted for approximately 40 minutes and transported approximately
237 1,050,000 m³ of sediment downstream. The deposition zone extended from the gully mouth to the
238 floodplain of the Niri River, covering a length of 320 m. The area measured from the UAV image
239 was approximately 0.15 km². The thickness of the sediment deposits ranged from 5 m to 15 m, with
240 an average value of 7 m. The debris flow flushed into the main river and blocked the Niri River.
241 The river channel was filled with sediment, which led to the formation of a dammed lake that raised
242 the water level by 7-8 m. After 40 minutes, the unstable dammed lake breached, which resulted in
243 a massive flash flood.



244
245 Figure 6 Distribution of maximum depth and velocity of the debris flow

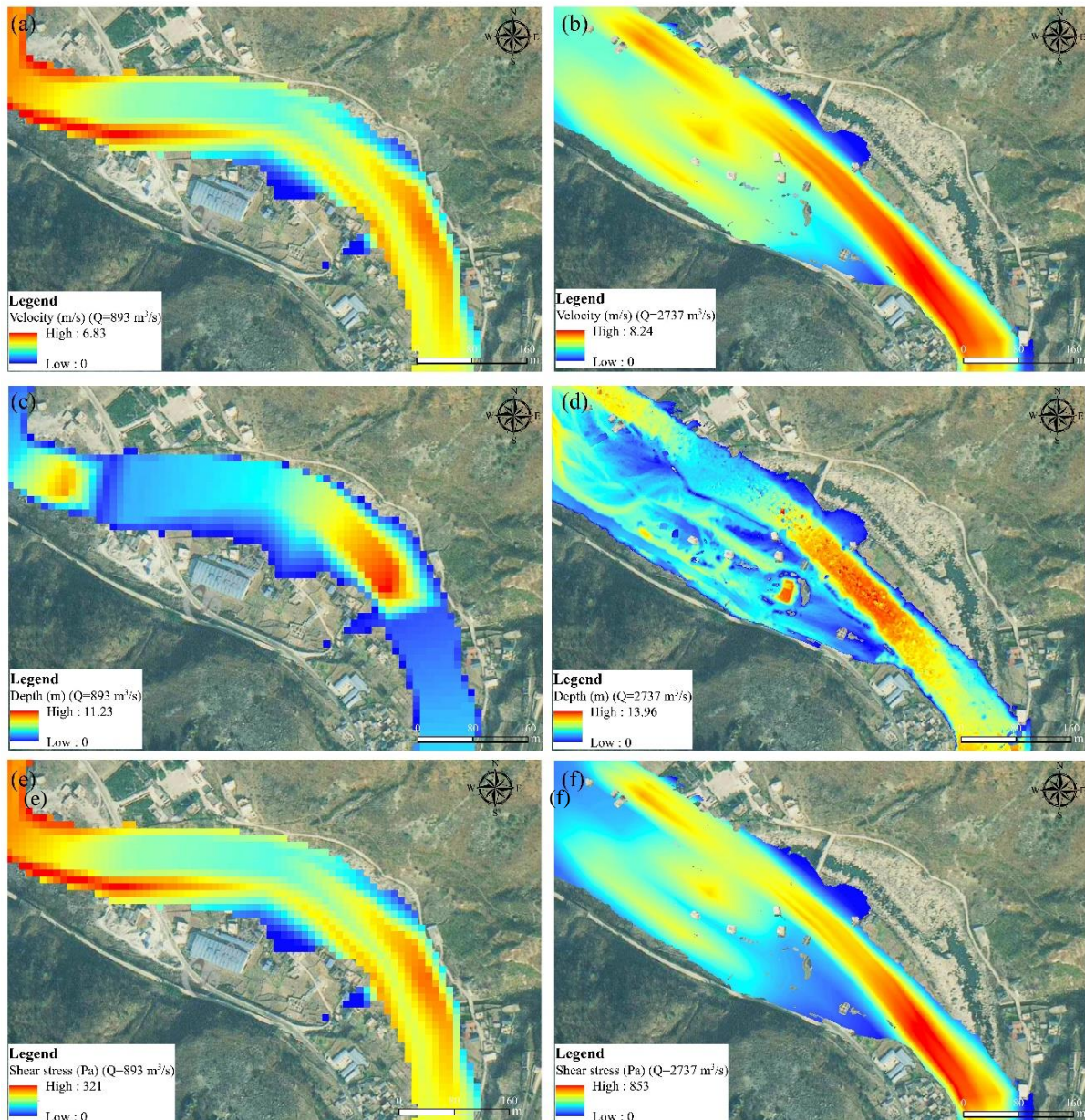
246 4.3 Dynamic characteristics of the outbreak flood

247 The outburst of the debris flow lake caused a sharp increase in flood peak discharge. To analyze
248 the dynamic characteristics of the flood caused by the dam burst, we first used Manning's hydraulic
249 formula for open channel flow (presented in Table 1) to calculate the peak discharge. Then, we
250 selected empirical formulas for dam-burst floods to verify the discharge. A typical section adjacent
251 to buildings damaged by the flood was chosen for the calculation (Fig. 4). Based on flood traces on
252 the outer walls of buildings and the damaged height of buildings, the flood depth was estimated to
253 be 6 m. The cross-sectional area and hydraulic radius were calculated according to the section
254 geometry and channel profile. The channel bed gradient was determined based on the longitudinal
255 channel profile. The resulting peak discharge was 2,737 m³/s. Field investigation revealed that the
256 height of the debris flow dam was approximately 12 m. The volume of the barrier lake was

257 calculated based on the terrain data collected before the disaster. The peak discharge was estimated
258 using the empirical formula proposed by Costa (1985) ($Q_{max} =$
259 $1.122V_s^{0.57}$, where V_s is the barrier lake volume), **resulting in a flow discharge of 2,273 m³/s with**
260 **a relative error of 18% which is comparable to the result obtained by Manning's equation.** The
261 temporal distributions of flood depth, velocity, and shear stress in the two scenarios are presented
262 in Fig. 7. The flood completely submerged all buildings on the left bank near the middle of the river
263 channel, and the buildings on the river terrace on the right bank were strongly eroded. The
264 maximum water depth and velocity of the dam-burst flood were 13.96 m and 8.24 m/s, respectively,
265 which were 1.24 and 1.31 times higher than those of the ordinary flood, respectively. The maximum
266 shear stress of the flood in the main channel increased sharply from 320 Pa to 853 Pa, indicating a
267 2.67-fold increase compared to the ordinary flood. For the ordinary flood scenario, the water depth
268 and velocity were high in the channel and decreased in the floodplain. In contrast, the high velocity
269 and shear stress zones that resulted from the dam-burst flood were mainly distributed in the main
270 channel and along the left bank, indicating that the material deposited by the debris flow and the
271 original river bank are highly susceptible to erosion.

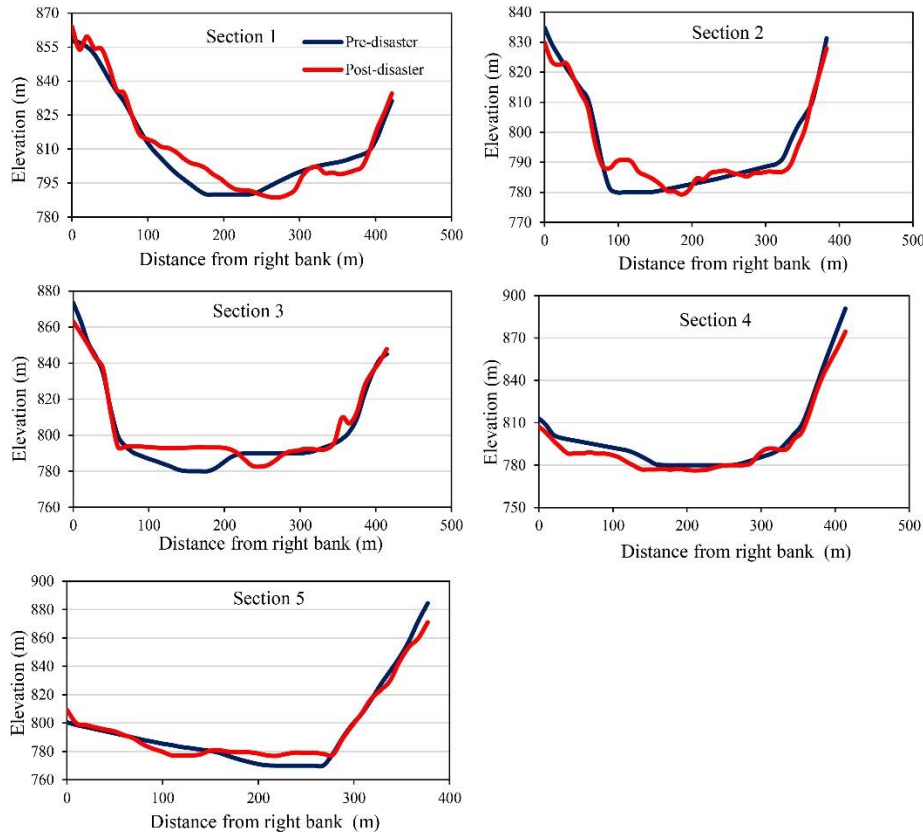
272 The critical shear stress for bedload transport in the gravel-bed river is determined by the equation
273 $\theta = \frac{\tau}{(\rho_s - \rho)gD} = 0.04$, where θ is the critical shear stress, τ is the bed shear stress, ρ_s is the soil mass
274 density, ρ is the water mass density, g is the gravitational acceleration, and D is the sediment
275 diameter (Petit et al., 2015). The dam-burst flood had the potential to transport large boulders up to
276 1.3 m in diameter, while an ordinary flood could only move gravel up to 0.49 m in diameter. Such
277 high shear stress also demonstrated the strong erosional ability of the dam-burst flood, which
278 seriously scoured the debris sediment deposit and original riverbank, transporting coarse gravel and
279 forming a new straight river channel. The new channel is straighter and steeper than the original
280 channel, raising the bed of the Niri River by 1-17 m and burying buildings up to 1 km downstream
281 of Heixluo Gully. The channel length shortened from 1010 m to 842 m, and the channel gradient
282 increased from 1.71% to 2.72%. The change in the river channel led to an inundation area that
283 deflected to the left. Buildings built on the original left riverbank were first impacted by debris flow
284 and subsequently destroyed by the flood. The river terrace on the original right bank was strongly
285 eroded by the flood, leading to the collapse and demolition of buildings. Five river sections (Section
286 1 to Section 5) were selected to analyze the terrain changes (see Fig. 4). From Section 1 to Section
287 3, the main channel varied from the right bank to the left bank with a distance between 40 m and
288 100 m, the average width of the new river channel was 50 m, and the vertical distance between the
289 new riverbed and floodplain was 11.23 m. In Section 5, the channel migrated from the left bank to

290 the right bank due to the severe erosion of the original river terrace and had a maximum depth of
 291 10 m (Fig. 8). The channel width increased to approximately 100 m, and the channel depth
 292 decreased to less than 5 m.



293
 294
 295
 296
 297
 298
 299

Figure 7 Distribution of depth, velocity, and shear stress of ordinary flood and dam-burst flood: (a) Maximum velocity distribution of ordinary flood; (b) Maximum velocity distribution of dam-burst flood; (c) Maximum depth distribution of ordinary flood; (d) Maximum depth distribution of dam-burst flood; (e) Maximum shear stress distribution of ordinary flood; (f) Maximum shear stress distribution of dam-burst flood.



300

301

Figure 8 Cross-section profile before and after the disaster.

302 **4.4 Damage patterns of buildings**

303 The debris flow-outburst flood hazard **cascade** caused damage to 108 buildings, a 1.2 km stretch
 304 of national road G245, and 5 highway bridges along the main river. The evolution of this hazard
 305 **cascade** occurred in two phases. First, the debris flow blocked the main river and formed a barrier
 306 dam and dammed lake, which was, second, followed by the outburst of the lake that led to the
 307 subsequent flooding and inundation. During the first phase, a significant amount of sediment was
 308 transported by the debris flow to the confluence area and deposited in the river channel, which
 309 formed a barrier lake with a volume of 857,504 m³. The barrier lake breached completely only
 310 approximately 40 minutes later, leading to a highly energetic flood that caused serious erosion of
 311 the riverbank and the formation of the outburst flood, a new straight river channel.

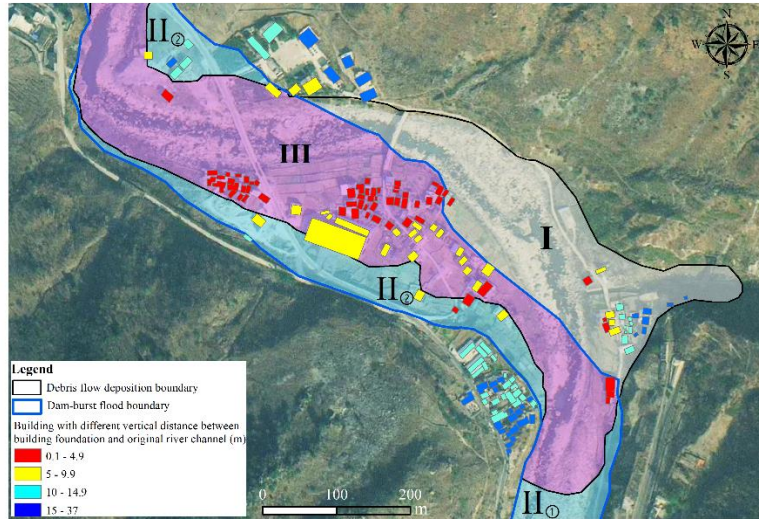
312 Fig. 9 illustrates the boundary of debris flow deposition and dam-burst flood inundation. The
 313 debris flow deposition boundary **was determined by the simulation**. **Flooding** boundary was
 314 obtained by combining the results of the HEC-RAS simulation with field survey data. The
 315 confluence area was heavily impacted by the debris flow, resulting in the transportation of a
 316 significant amount of solid materials over an area of 0.157 km². As a result, the majority of the

317 village's buildings were inundated by the debris flow. The dam-burst flood caused serious damage
318 to buildings by flushing a large volume of debris flow sediment and riverbank material downstream.

319 Three hazard zones are identified based on the boundary of the debris flow and dam-burst flood,
320 as shown in Fig. 9 and Fig. 10. The damage patterns of buildings in the different hazard zones can
321 be classified into three categories, namely, (I) buildings only buried by debris flow; (II) buildings
322 only inundated by dam-burst flood; and (III) buildings sequentially buried by debris flow and
323 inundated by dam-burst flood. Zone (I) is situated near the Heixiluo gully mouth, where the debris
324 flow transported a large volume of sediment and seriously eroded the sidewall and bed of the
325 channel, expanding the channel's width from 10 m to 40 m. All buildings were inundated by
326 sediment to a depth of over 6 m.

327 Zone (II) is subdivided into two subzones, Zone (II) ① and Zone (II) ②, based on the spatial
328 location. Zone (II) ① is situated in the upstream reach of the Niri River, near the debris flow dam,
329 and is mainly inundated by the static water of the dammed lake (Fig. 10(b)). Zone (II) ② lies on the
330 right bank of the downstream reach of the Niri River, outside the debris flow fan. The original right
331 riverbank in Zone (II) ② was a terrace 10 m high that was severely scoured by the highly energetic
332 flood with a shear stress greater than 450 Pa. The entire terrace was cut off, and a new channel was
333 formed across the middle area (Fig. 10(c)). The erosion area on the river terrace measures
334 approximately 1800 m² with a length of 300 m and a width of 60 m. Two buildings situated on the
335 upper part of the river terrace collapsed and disintegrated due to the impact of the flood (part (a) in
336 Fig. 10(d)). A three-story building was partially destroyed due to foundation erosion. The buildings
337 on the lower part of Zone (II) ② were simultaneously buried by the sediment transported by floods
338 and inundated by floodwater (part (b) in Fig. 10(d)).

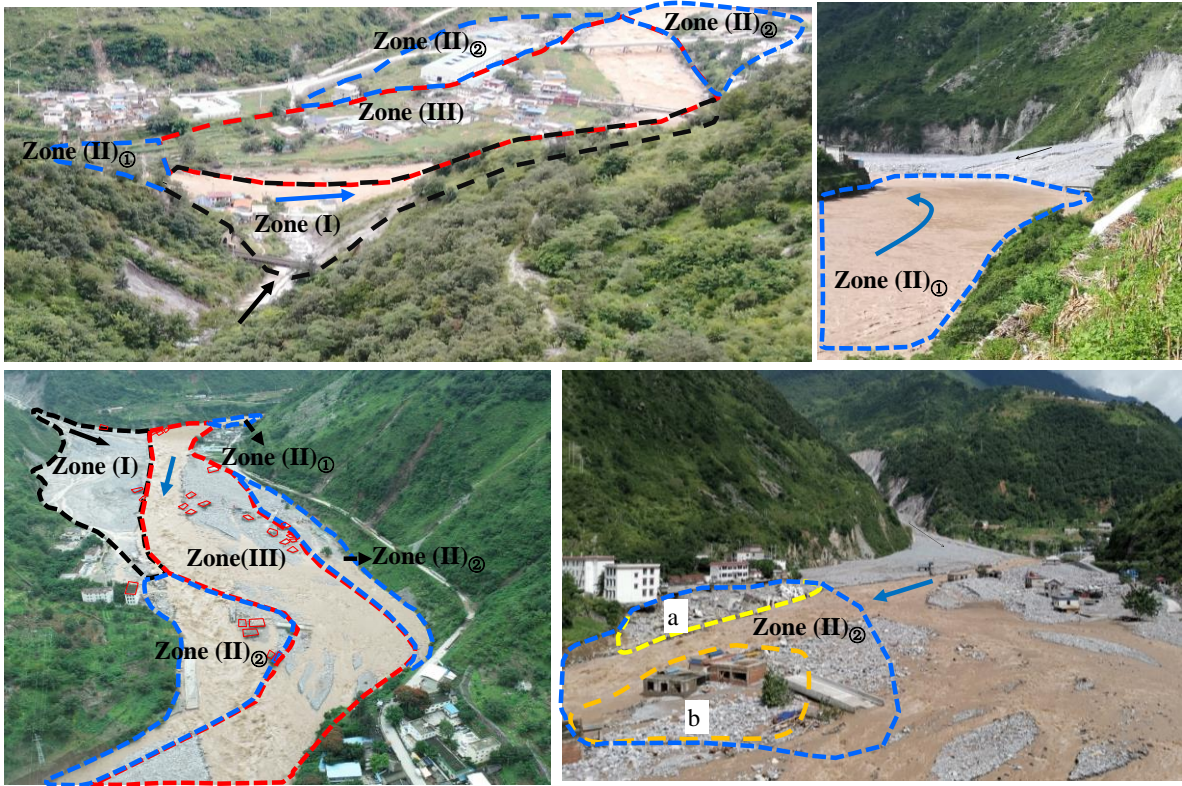
339 Zone (III) is primarily located on the left bank of the original river and the lower part of the
340 debris flow fan. The original river channel is filled with debris up to a depth of 10 m. The debris
341 flow transported sediment across the raised riverbed into villages and formed a slope that was high
342 on the right and low on the left in the confluence area. Then, the flood breached the debris flow
343 dam and severely eroded the deposited debris and the original floodplain surface, resulting in a new
344 straight channel. The buildings on the left bank of the river, which were buried by the debris flow,
345 were sequentially impacted by the dam-breach flood. The flood heavily damaged buildings near
346 the new river channel and floodwater from the channel was observed to always inundate the
347 buildings. Notably, the boundaries of the different damage zones are not static. The extent of the
348 damage zone is not the same for other confluence areas; it is determined by the dynamic
349 characteristics of hazards and is also influenced by the local terrain.



350
 351 **Figure 9** Inundation boundary of debris flow and dam-burst flood and spatial division of the hazard zone
 352 based on building damage patterns: (I) buried by debris flow; (II) inundated by dam-burst flood; (III)
 353 buried by debris flow and the inundated by dam-burst flood.
 354 A total of 108 buildings in the village were impacted by the multi-hazards, accounting for 67.9%
 355 of the total buildings. Among them, 75 buildings located in Zone (III) were impacted by the debris
 356 flow and flood in succession, which accounted for 47.2% of the total buildings. In contrast,
 357 buildings destroyed by the debris flow in Zone (I) and dam-burst flood in Zone (II) accounted for
 358 only 15.1% and 5.7% of the total buildings, respectively (Table 4). Overall, the number of buildings
 359 within the debris flow deposition boundary and flood inundation boundary is 99 and 84,
 360 respectively, accounting for 63.5 % and 53.8% of the total buildings in the village.

361 The impact force of fluvial sediment transport is greatly influenced by the relative distance of
 362 buildings to channels (Wei et al., 2022). Buildings that are close to the channel are always more
 363 vulnerable to damage than those located farther away from the river. During the hazard cascade, a
 364 total of 84 buildings in Zone (II) and Zone (III) were impacted by the dam-burst flood (Fig. 10).
 365 To assess the influence of building distance from the river channel, we analyzed the vertical
 366 distances between the damaged building foundation and the original river channel based on pre-
 367 event terrain (Table 5). We found that 67.86% of all damaged buildings were within 5 m of the
 368 channel, while 23.81% of all damaged buildings were between 5 m and 10 m of the original channel.
 369 Buildings that were located at distances greater than 10 m only accounted for 8.33% of the total
 370 damaged buildings. In contrast, the average vertical distance of undamaged buildings was 15.3 m,
 371 with a minimum value of 11.4 m.

372



373
374
375
376

Figure 10 Spatial distribution of the three hazard zones before and after the disaster: (a) before the disaster; (b) (c) (d) after the disaster.

Table 4 Statistics of buildings damaged by the debris flow and dam-burst flood

Damage pattern	(I) Buried by debris flow	(II) Inundated by dam-burst flood	(III) Buried by debris flow and inundated by dam-burst flood sequentially	Sum
Total number of buildings destroyed	24	9	75	108
The proportion of damaged buildings to the total buildings in the village (%)	15.1	56.6	47.2	67.9

377
378
379

Table 5 Statistics of the vertical distance between the damaged building foundation and original river channel within the whole flooding boundary

The vertical distance between the building foundation and original river channel (m)	(0, 5)	(5,10)	(10,16)	Sum
Total number of buildings destroyed	57	20	7	84
The proportion of damaged buildings to the total (%)	67.86	23.81	8.33	100

380 4.5 Vulnerability analysis of the buildings

381 Most of the buildings in the village were completely buried by sediments or collapsed with no
382 visible remains. To construct vulnerability curves, 29 damaged buildings with brick-concrete

383 structures located in the three hazard zones were selected (Fig. 10(c), Fig. 11). Of these, 6 buildings
384 were located in Zone (II), and the rest were distributed throughout Zone (III).

385 The building characteristics and hazard intensity are presented in Table 6. In Zone (III),
386 buildings located near the debris flow dam (such as buildings 1, 2, and 3) were first buried by the
387 debris flow and then inundated by water from the dammed lake for 40 minutes. These buildings
388 were then impacted by the dam-burst flood. Additionally, buildings near the new river channel
389 suffered greater impact pressure than other buildings. For example, the residual broken structures
390 of buildings 5 and 6 were heavily damaged by the direct impact of the flood in the vertical direction.
391 The walls of the two buildings were severely abraded by impact pressures of 75.5 kPa and 71.1
392 kPa, respectively. Additionally, the foundations of the two buildings were partially scoured by
393 floods with high shear stresses of 562 Pa and 553 Pa, respectively.

394 Buildings located in Zone (II) were only severely impacted by the dam-burst flood. For instance,
395 the foundation of the three-story school building (building 26) was severely eroded by the flood to
396 a scour depth of 1 m, and the floors on the right collapsed. There was no evidence on the walls of
397 the building that the debris flow had abraded the structure. The velocity and shear stress of the
398 flood in this location were 4.4 m/s and 463 Pa, respectively. Buildings 23-25, which were close to
399 the new river channel, were thoroughly buried by the sediment transported by the flood and
400 inundated by floodwater.

401



402
403

Figure 11 Buildings with different degrees of damage within three hazard zones.

Table 6 Database of the damaged buildings

Building	Debris flow deposition depth (m)	Debris flow velocity (m/s)	Debris flow impact pressure (kPa)	Flood depth (m)	Flood velocity (m/s)	Flood impact pressure (kPa)	Damage ratio	Hazard zone
1	4.0	0.5	36.8	1.2	1.0	7.0	0.7	III
2	3.7	0.4	33.8	1.3	2.0	10.3	0.6	III
3	3.2	0.3	28.8	1.3	2.3	11.6	0.6	III
4	5.5	1.8	55.2	3.7	4.3	36.8	0.8	III
5	5.7	1.5	55.3	6.7	6.5	75.5	1	III
6	7.0	2.0	69.7	6.3	6.3	71.1	1	III
7	3.9	0.9	36.2	2.1	4.1	27.3	0.6	III
8	5.1	1.4	49.2	6.4	6.7	76.6	1	III
9	4.9	1.3	47.3	6.3	6.0	67.1	1	III
10	3.5	0.9	32.5	0.9	3.6	17.6	0.7	III
11	5.3	1.4	51.2	4.4	5.9	56.3	1	III
12	5.1	1.4	48.7	3.6	5.1	43.3	0.7	III
13	2.5	0.6	22.9	0.7	1.5	5.8	0.4	III
14	2.3	0.6	21.5	1.2	0.8	6.5	0.3	III
15	1.9	0.4	17.0	3.0	4.6	35.7	1	III
16	1.3	0.3	12.1	3.9	5.0	44.4	1	III
17	2.5	0.8	23.8	2.4	3.8	26.0	0.7	III
18	3.0	1.2	29.3	2.4	4.1	28.1	0.9	III
19	2.3	1.1	22.2	3.5	4.7	39.5	1	III
20	0.9	0.1	7.7	5.1	5.1	51.4	1	III
21	1.2	0.3	11.2	3.7	3.6	31.5	0.7	III
22				1.62	3.20	10.3	0.4	II
23				4.74	4.89	55.3	0.8	II
24				3.72	3.64	18.2	0.7	II
25				3.66	5.27	47.2	0.8	II
26				4.47	4.37	45.8	0.9	II
27				5.09	5.14	41.0	1	II

405 The vulnerability curve in Zone (II) and Zone (III) was developed by summing up the damage
406 caused by the multiple hazards and impact pressure (Fig. 12). Logistic functions were proposed
407 separately for the two hazard zones, and the corresponding determination coefficient (R^2) and root
408 mean square error (RMSE) were also obtained. The determination coefficients of the two regression
409 curves in Zone (III) have a higher R^2 . The RMSEs of the curves in Zone (II) and Zone (III) are 0.36
410 and 0.68, respectively. The correlation between vulnerability and inundation depth in the two zones
411 is shown in Fig. 13, with an R^2 lower than impact pressure ($R^2=0.59$ for Zone (II) and $R^2=0.30$ for
412 Zone (III)). Building vulnerability increases with increasing hazard intensity, and the trend is similar
413 in the two zones. The impact pressure thresholds for Zones II and III, where vulnerability is equal

414 to 1, are 75 kPa and 110 kPa, respectively. For the same impact pressure and inundation depth, the
 415 damage to buildings in Zone (II) is greater than that in Zone (III).

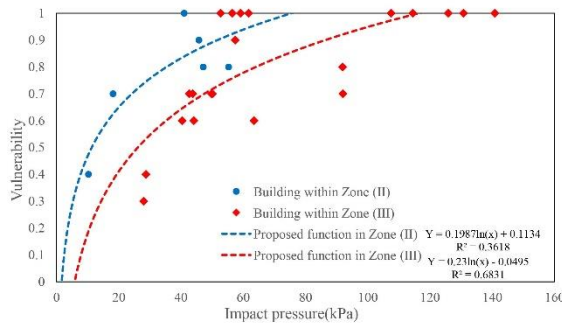


Figure 12 Proposed vulnerability functions based on the impact pressure in Zone (II) and Zone (III).

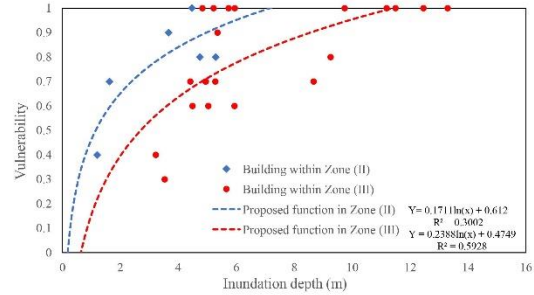


Figure 13 Proposed vulnerability functions based on the inundation depth in Zone (II) and Zone (III).

416 The vulnerability curves proposed for Zone (II) and Zone (III) were compared to the three
 417 functions used in debris flow risk assessment (Fig.14, Fig.15). The functions developed by [Quan](#)
 418 [et al. \(2011\)](#) and [Kang et al. \(2016\)](#) were calculated based on damage done to brick masonry and
 419 nonreinforced concrete structures that had been impacted by the debris flows in South Korea and
 420 Italy, respectively. The vulnerability curve proposed by [Zhang et al. \(2018\)](#) was developed for
 421 buildings with brick-concrete structures from the Zhouqu debris flow event in China. The slope of
 422 the two proposed vulnerability curves based on impact pressure is smaller than those of the three
 423 curves. When the impact pressure is less than 20 kPa, the proposed curves show a similar increasing
 424 trend compared to the three functions. However, when the impact pressure is greater than 20 kPa,
 425 the slope of the two proposed vulnerability curves is much smaller than those of the three curves.
 426 For the curves based on inundation depth, when the depth is less than 1.5 m, the slope is steeper
 427 than that of [Quan et al. \(2011\)](#) and [Zhang et al. \(2018\)](#) and slower than that of [Kang et al. \(2016\)](#).
 428 When the depth is greater than 2 m, the damage increases slower than the curves of [Quan et al.](#)
 429 [\(2011\)](#) and [Zhang et al. \(2018\)](#). This disparity may be attributed to the different damage patterns
 430 and structures of the buildings in this study. The three vulnerability functions were generated for a
 431 single debris flow event, whereas the mechanisms by which buildings impacted by floods fail are
 432 not the same when those buildings are subjected to a debris flow. The structures of most buildings
 433 in the study area are tougher than those in the three events, and nearly half of the buildings had
 434 been recently built by a more professional construction team. For example, the newly built four
 435 **building 7** was not completely damaged by hazard **cascade** under impact pressures greater than 63.5
 436 kPa.

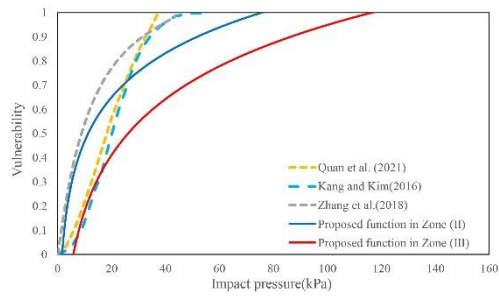


Figure 14 Comparison of the building vulnerability functions with the impact pressure functions proposed by Quan et al. (2011), Kang et al. (2016), and Zhang et al. (2018).

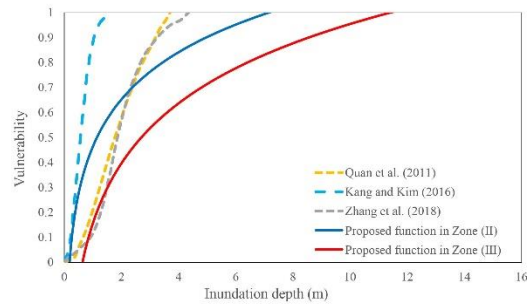
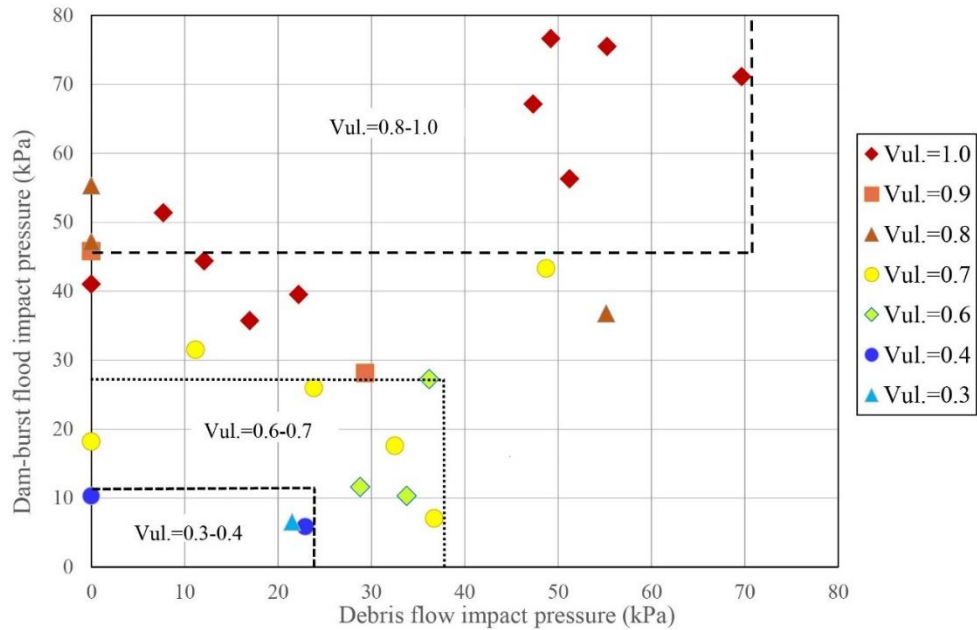


Figure 15 Comparison of the building vulnerability functions with the inundation depth proposed by Quan et al. (2011), Kang et al. (2016), and Zhang et al. (2018).

437 The building damage distribution chart shows building damage plotted as a function of debris
 438 flow and flood impact pressure (see Fig. 16). The figure includes aggregated damage to buildings
 439 impacted by the sequentially occurring hazards in Zone (III) and damage caused by a single hazard
 440 in Zone (II). Damage is divided into three categories based on the threshold impact pressure: slight
 441 damage (0.3-0.4), moderate damage (0.6-0.7), and heavy and complete damage (0.8-1.0). Heavy
 442 and complete damage mainly occurs at impact pressures greater than 60 kPa.

443 , while slight damage occurs below 30 kPa. Moderate damage mainly occurs at impact pressures
 444 between 40 kPa and 60 kPa. The threshold impact pressure is compared with that proposed by Hu
 445 et al. (2012) and Zanchetta et al. (2004), which were derived from a single debris flow disaster in
 446 China and Italy, respectively. Although the detailed definition of the damage scales differs, the
 447 threshold of the impact pressure for buildings at the slight, heavy, and complete damage scales is
 448 generally larger than that for the brick-concrete structures presented in Hu et al. (2012) and smaller
 449 than that for the reinforced concrete frames also presented in Hu et al. (2012) and the masonry
 450 structures with basements presented in Zanchetta et al. (2004). A similar trend for the threshold of
 451 the impact pressure for buildings with a moderate damage scale can be observed.



452

453

Figure 16 Accumulation of building damage due to debris flow and dam-burst flood. The damage distribution is based on the debris flow and flood impact pressure (Vul. refers to vulnerability).

454

455

456

457

458

459

460

461

462

463

464

465

466

467

468

The building damage distribution chart remains a valid tool for assessing the vulnerability of buildings affected by debris flows and flash floods, despite not incorporating all damage ratios. However, some limitations and uncertainties exist within the vulnerability functions. For instance, calculating a single average impact pressure value prebuilding for building clusters introduces uncertainty, as water depth and velocity differ significantly at different sides of the building due to the shielding effect (Hu et al., 2012; Arrighi et al., 2020). Furthermore, the building's geometry, direction, orientation, and maintenance condition are not considered in the vulnerability analysis. The amplification of debris flow damage is due to subsequent flooding in time and space. Aggregated damage (i.e., damage caused by both debris flows and floods) is applied in the vulnerability analysis for areas that are successively struck by debris flows and floods. However, the amplified damage effect of the dam-burst flood on debris flow was not accurately quantified because of the absence of a database containing information regarding the damage done by the debris flow before the dam burst. As a result, more detailed data are needed to assess the cumulative impact of hazard cascades on building vulnerability.

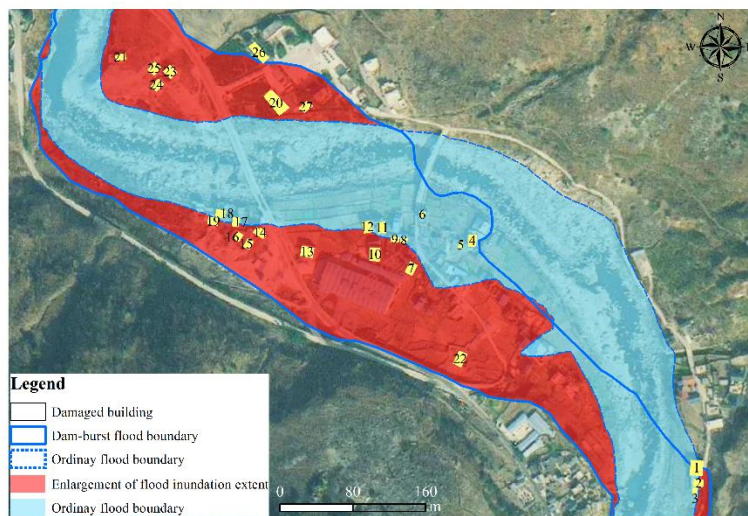
469 **5 Discussion**

470 **5.1 Damage aggravation due to hazard cascade**

471 As a result of the confluence zone's location on a river bend, the dam-burst flood typically flows
472 in a straight direction and creates a new straight channel when the river channel becomes
473 completely blocked. This channel translocation leads to a larger flooded area and causes more
474 severe damage to buildings on the floodplain. The flood inundation zones in the village expanded
475 to 110^5 m^2 , which is up to 4 times the area of an ordinary flood due to flood amplification (Fig. 17).
476 In the expanded inundation zone, 41 buildings, a traffic road spanning 410 m, and farmland with
477 an area of $10 \times 10^4 \text{ m}^2$ were submerged. The buildings located in the middle of the inundation zones
478 suffered the most severe damage due to the floodwater's high scouring capability and sediment
479 transport capacity. Many buildings near the flow collapsed, and most structures were carried away
480 by the water current.

481 Table 7 presents a comparison of the dynamic characteristics and damage increments between
482 ordinary and dam-burst floods in different locations. The damage increment is calculated based on
483 the proposed function in Zone II and is the ratio of the damage caused by the two floods. Buildings
484 4, 5, 6, 9, 11, 18, and 19 were situated close to the new river channel, and the average bed shear
485 stress and impact pressure increased up to 14.2 times and 3.8 times that of an ordinary flood,
486 respectively, due to flood amplification. The average damage to the seven buildings located near
487 the new channel increased by 140% due to the lake created by the debris flow barrier.

488



489

490

Figure 17 The inundation extent of ordinary floods and dam-burst floods.

491

Table 7 Comparison of dynamic characteristics and degree of damage between ordinary floods and dam-burst floods in different locations

492

Location	The ratio of dam-burst flood to ordinary flood				
	Depth	Velocity	Bed shear stress	Impact pressure	Damage degree
Building 4	1.5	1.5	8.3	1.9	1.2
Building 5	0.8	2.0	13.1	2.0	1.2
Building 6	2.3	1.7	11.8	2.5	1.3
Building 9	15.0	3.2	33.8	11.2	2.4
Building 11	4.6	2.2	19.0	4.9	1.6
Building 18	2.6	1.1	6.2	1.5	1.1
Building 19	18.6	1.3	7.4	2.7	1.3
Average value	6.5	1.9	14.2	3.8	1.4

493 **5.2 The implication of hazard mitigation**

494 In recent years, the hazard **cascade** of debris flows and outburst floods has become more frequent
495 in high mountain regions due to the impact of climate change and earthquakes (Chen et al., 2022).
496 The damage caused by the primary debris flow can be intensified and enlarged due to the successive
497 dam-burst flood.

498 Risk assessment for debris flow-outburst flood hazard **cascades** is crucial to mitigate the damage
499 posed to structures in the confluence zone. Risk analysis should incorporate both the debris flow
500 initiation mechanism and the mechanism that generates the dam-burst flood (Chen et al., 2022). A
501 detailed investigation should be conducted for the exposed elements in the confluence zone and in
502 both the upstream and downstream reaches of the river. Based on the disaster transformation
503 process and the failure mechanisms of structures, hazard zones should be identified, and
504 corresponding disaster reduction measures should be developed (Cui and Guo, 2021). Moreover,
505 specific structural measures are urgently needed. First, engineering measures should be
506 implemented in the watershed to mitigate debris flows (Cui and Lin, 2013). Second, buildings
507 should not be constructed near debris flow gullies, and new buildings should be built on elevated
508 ground or at certain elevations above the ground (Attems et al., 2019). Third, deflection walls
509 should be considered and constructed in villages susceptible to debris flows to protect entire
510 buildings (Wang et al., 2022), and flood protection walls should be built along the main river to
511 protect the entire flood-prone village.

512 This study presents a comprehensive analysis of the damage to buildings resulting from a large-
513 scale debris flow and outburst flood hazard cascade. The study develops building vulnerability in
514 different areas of the confluence zone, which is useful for building risk assessment and management
515 along the riverbank. However, some uncertainties and limitations are involved in vulnerability
516 analysis. Firstly, the study did not consider the building's physical characteristics, such as shape,
517 orientation, and maintenance condition. Secondly, in the area affected by the two hazards, the

518 capacity of buildings first damaged by debris flow had declined, leading to a higher failure
519 probability under the impact of sequential flood (Luo et al., 2020). The study analyzed the
520 buildings' structural vulnerability based on debris flows and dam-break flood separately, and did
521 not consider the building response to the primary debris flow or quantify the cumulative effect of
522 the debris flow and the dam-break flood (Luo et al., 2023). A physics-based vulnerability model is
523 required to quantify the dynamic evolution of building vulnerability.

524 **6 Conclusions**

525 Buildings in the confluence zone of a debris flow-prone catchment and along a main river
526 channel are highly vulnerable to a debris flow-dam-burst flood hazard **cascade**. Assessing building
527 damage is essential for risk mitigation and resilient construction. However, research concerning
528 building damage mainly focuses on a single debris flow or flash flood and fails to consider the
529 different damage characteristics of buildings exposed to both hazards simultaneously. Therefore,
530 studying the characteristics and patterns of building damage in confluence areas can help to develop
531 a reliable vulnerability assessment method. In this study, we investigate the dynamic characteristics
532 of the hazards and damage patterns of the 2020 Heixiluo debris flow and dam-burst flood disaster.
533 We draw the following conclusion:

534 1. The dam-burst flood, which had a peak discharge of **2,737** m³/s, seriously eroded the debris
535 flow fan and formed a new straighter and steeper channel. The maximum estimated velocity was
536 8.24 m/s, and the bed shear stress reached 853 Pa. The flood's inundation extent in the confluence
537 zone was expanded by a factor of 4, and the impact pressure increased up to **6.8** times due to flood
538 amplification. **The average damage to buildings near the new river channel was 1.4 times more**
539 **intense due to the hazard cascade.**

540 2. The damage patterns of the buildings were classified into three types: (I) buried by primary
541 debris flow, (II) inundated by secondary dam-burst flood, and (III) buried by debris flow and
542 inundated by dam-burst flood sequentially. The spatial division of hazard zones can be applied to
543 the selection of building sites and the planning of structural measures in the confluence area.

544 3. The vulnerability curves show a similar increasing trend with impact pressure and inundation
545 depth in Zones II and III, and the threshold of the impact pressures in Zones II and III where
546 vulnerability is equal to 1 is **75 kPa and 110 kPa**, respectively. A vulnerability assessment chart
547 was developed, and three categories, namely, slight damage (0.3-0.4), moderate damage (0.6-0.7),
548 and heavy and complete damage (0.8-1.0), were identified. Heavy damage occurs at an impact
549 pressure greater than 40 kPa, while slight damage occurs below **30 kPa**. Moderate damage occurs
550 at an impact pressure between **40 kPa and 60 kPa**.

551 4. Some uncertainties and limitations are involved in vulnerability analysis. The building's
552 physical characteristics, such as shape, orientation, and maintenance condition, should be
553 considered for the vulnerability analysis. Further investigation and research are recommended to
554 explore the cumulative effect of multiple hazards on building vulnerability. Despite the deficiencies,
555 vulnerability curves, and assessment charts are valuable for analyzing the risk posed by debris flow
556 hazard cascades within the confluence zone.

557

558 **Acknowledgments**

559 This work has been financially supported by the the Second Tibetan Plateau Scientific Expedition
560 and Research Program (2019QZKK0902) and the National Natural Science Foundation of China
561 (41790434).

562

563 **Data availability**

564 All raw data can be provided by the corresponding authors upon request.

565

566 **Author contributions**

567 Kaiheng Hu contributed to the conception of the study; Li Wei performed the data analyses and
568 wrote the manuscript draft; Shuang Liu performed the data analyses. Lan Ning, Xiaopeng Zhang
569 and Qiyuan Zhang performed the field investigation; Md Abdur Rahim reviewed and edited the
570 manuscript.

571

572 **Competing interests.**

573 The authors declare that they have no conflict of interest.

574

575

576 **References**

- 577 Argyroudis, S. A., Mitoulis, S. A., Winter, M. G., and Kaynia, A. M.: Fragility of transport assets exposed
578 to multiple hazards: State-of-the-art review toward infrastructural resilience, *Reliability Engineering*
579 *and System Safety*, 191, 106567, <https://doi.org/10.1016/j.ress.2019.106567>, 2019.
- 580 Arrighi, C., Mazzanti, B., Pistone, F., and Castelli, F.: Empirical flash flood vulnerability functions for
581 residential buildings. *SN Applied Sciences*, 2, 904, <https://doi.org/10.1007/s42452-020-2696-1>, 2020.
- 582 Attems, M. S., Thaler, T., Genovese, E., and Fuchs, S.: Implementation of property-level flood risk adaptation
583 (PLFRA) measures: Choices and decisions. *Wiley Interdisciplinary Reviews, Water*, 7(1), e1404,
584 <https://doi.org/10.1002/wat2.1404>, 2020.
- 585 Chen, H., Ruan, H., Chen, J., Li, X., and Yu, Y.: Review of investigations on hazard cascades triggered by
586 river-blocking debris flows and dam-break floods, *Frontiers in Earth Science*, 10, 582.
587 <https://doi.org/10.3389/feart.2022.830044>, 2022. Costa, J.E.: *Floods from Dam Failures*, Open-File Rep.
588 No. 85–560. U.S. Geological Survey, Denver, 1985.
- 589 Cui P., and Guo J.: Evolution models, risk prevention and control countermeasures of the valley disaster
590 chain, *Advanced Engineering Sciences*, 53(3), 5-18 <https://doi.org/10.15961/j.jsuese.202100285>, 2021.
- 591 Cui, P., and Lin, Y.M.: Debris-flow treatment: The integration of botanical and geotechnical methods, *Journal*
592 *of Resources and Ecology*, 4(2), 97-104. <https://doi.org/10.5814/j.issn.1674-764x.2013.02.001>, 2013.
- 593 Cutter, S. L. (2018). Compound, cascading, or complex disasters: what's in a name? *Environment: Science*
594 *and Policy for Sustainable Development*, 60(6), 16-25.
- 595 Gallina, V., Torresan, S., Critto, A., Sperotto, A., Glade, T., and Marcomini, A.: A review of multi-risk
596 methodologies for natural hazards: Consequences and challenges for a climate change impact
597 assessment, *Journal of environmental management*, 168, 123-132,
598 <https://doi.org/10.1016/j.jenvman.2015.11.011>, 2016.
- 599 Gautam, D., and Dong, Y.: Multi-hazard vulnerability of structures and lifelines due to the 2015 Gorkha
600 earthquake and 2017 central Nepal flash flood. *Journal of Building Engineering*, 17, 196-201.
601 <https://doi.org/10.1016/j.jobe.2018.02.016>, 2018.
- 602 He, Y. B., Xu, Y.N. and Zhang, J.: Analysis of flood control effect of Pubugou Reservoir during “20•8” flood
603 of Minjiang River, *Yangtze River*, 51(12):149-154, [https://doi.org/10.16232/j.cnki.1001-4179.2020.12.](https://doi.org/10.16232/j.cnki.1001-4179.2020.12.027)
604 027, 2020.
- 605 Hu, K. H., Cui, P., and Zhang, J. Q.: Characteristics of damage to buildings by debris flows on 7 August
606 2010 in Zhouqu, Western China, *Natural Hazards and Earth System Sciences*, 12(7), 2209-2217.
607 <https://doi.org/10.1016/10.5194/nhess-12-2209-2012>, 2012.
- 608 Hu, G., Tian, S., Chen, N., Liu, M., and Somos-Valenzuela, M.: An effectiveness evaluation method for
609 debris flow control engineering for cascading hydropower stations along the Jinsha River, China,
610 *Engineering Geology*, 266, 105472, <https://doi.org/10.1016/j.enggeo.2019.105472>, 2020.
- 611 Hydrologic Engineering Center: HEC-RAS, River Analysis System, *Hydraulics Reference Manual*, Version.
612 5.0. Davis, California, U.S. Army Corps of Engineers 25 (2016).

613 Kang, H. S., and Kim, Y. T.: The physical vulnerability of different types of building structure to debris flow
614 events, *Natural Hazards*, 80, 1475-1493, <https://doi.org/10.1007/s11069-015-2032-z>, 2016.

615 Kang, Z.C., Li, Z.F., Ma, A.N.: Debris flows in China. Science, Beijing(in Chinese), 2004.

616 Kang, Z.C.: A velocity research of debris flow and its calculating method in China, *Mountain Research*, 5
617 (4), 247–259, 1987. (in Chinese).

618 Kappes, M. S., Keiler, M., von Elverfeldt, K., and Glade, T.: Challenges of analyzing multi-hazard risk: a
619 review, *Natural hazards*, 64, 1925-1958. <https://doi.org/10.1007/s11069-012-0294-2>, 2012.

620 Korswagen, P. A., Jonkman, S. N., and Terwel, K. C.: Probabilistic assessment of structural damage from
621 coupled multi-hazards, *Structural safety*, 76, 135-148, <https://doi.org/10.1016/j.strusafe.2018.08.001>,
622 2019.

623 Liu, Z., Nadim, F., Garcia-Aristizabal, A., Mignan, A., Fleming, K., and Luna, B. Q.: A three-level
624 framework for multi-risk assessment, *Georisk: Assessment and management of risk for engineered*
625 *systems and geohazards*, 9(2), 59-74, <https://doi.org/10.1080/17499518.2015.1041989>, 2015.

626 Luo, H. Y., Zhang, L. M., Zhang, L. L., He, J., and Yin, K. S.: Vulnerability of buildings to landslides, The
627 state of the art and future needs. *Earth-Science Reviews*, 104329,
628 <https://doi.org/10.1016/j.earscirev.2023.104329>, 2023.

629 Luo, H., Zhang, L., Wang, H., and He, J.: Multi-hazard vulnerability of buildings to debris flows, *Engineering*
630 *Geology*, 279, 105859, <https://doi.org/10.1016/j.enggeo.2020.105859>, 2020.

631 Ning, L., Hu, K., Wang, Z., Luo, H., Qin, H., Zhang, X., and Liu, S.: Multi-hazard cascade reaction initiated
632 by the 2020 Meilong debris flow in the Dadu River, Southwest China. *Frontiers in Earth Science*, 10,
633 827438, <https://doi.org/10.3389/feart.2022.827438>, 2022.

634 Park, S., van de Lindt, J. W., Cox, D., Gupta, R., and Aguiniga, F.: Successive earthquake-tsunami analysis
635 to develop collapse fragilities, *Journal of Earthquake Engineering*, 16(6), 851-863,
636 <https://doi.org/10.1080/13632469.2012.685209>, 2012.

637 Petit, F., Houbrechts, G., Peeters, A., Hallot, E., Van Campenhout, J., and Denis, A. C.: Dimensionless
638 critical shear stress in gravel-bed rivers, *Geomorphology*, 250, 308-320.
639 <https://dx.doi.org/10.1016/j.geomorph.2015.09.008>, 2015.

640 Petrone, C., Rossetto, T., Baiguera, M., De la Barra Bustamante, C., and Ioannou, I.: Fragility functions for
641 a reinforced concrete structure subjected to earthquake and tsunami in sequence, *Engineering Structures*,
642 205, 110120, <https://doi.org/10.1016/j.engstruct.2019.110120>, 2020.

643 Quan, L.B., Blahut, J., van Westen, C.J., Sterlacchini, S., van Asch, T.W.J., Akbas, S.O.: The application of
644 numerical debris flow modelling for the generation of physical vulnerability curves, *Natural Hazards*
645 *and Earth System Sciences*, 11, 2047-2060, <https://doi.org/10.5194/nhess-11-2047-2011>, 2011.

646 Tilloy, A., Malamud, B. D., Winter, H., and Joly-Laugel, A.: A review of quantification methodologies for
647 multi-hazard interrelationships, *Earth-Science Reviews*, 196, 102881,
648 <https://doi.org/10.1016/j.earscirev.2019.102881>, 2019.

649 Wang, J., Hassan, M. A., Saletti, M., Yang, X., Zhou, H., and Zhou, J.: Experimental study on the mitigation
650 effects of deflection walls on debris flow hazards at the confluence of tributary and main river, *Bulletin*
651 *of Engineering Geology and the Environment*, 81(9), 354.

652 Wei, L., Hu, K., and Liu, J.: Automatic identification of buildings vulnerable to debris flows in Sichuan
653 Province, China, by GIS analysis and Deep Encoding Network methods, *Journal of Flood Risk*
654 *Management*, 15(4), e12830, <https://doi.org/10.1111/jfr3.12830>, 2022.

655 Xu, L., Meng, X. and Xu, X.: Natural hazard cascade research in China: A review, *Natural Hazards* 70, 1631-
656 1659 , <https://doi.org/10.1007/s11069-013-0881-x>, 2014.

657 Yan, Y., Cui, Y., Liu, D., Tang, H., Li, Y., Tian, X., Zhang, L., and Hu, S.: Seismic signal characteristics and
658 interpretation of the 2020 “6.17” Danba landslide dam failure hazard cascade process, *Landslides*, 18,
659 2175–2192 (2021). <https://doi.org/10.1007/s10346-021-01657-x>, 2021.

660 Yang, Z.N., 1985. Preliminary study on the flowing velocity of viscous debris flows due to intense rainfall,
661 *Research of debris flows*, *Proceeding of the Lanzhou Institute of Glaciology and Cryopedology*, Chinese
662 *Academy of Sciences*. No. 4. Science Press, Beijing (in Chinese).

663 Yu, B., Ma, Y., and Wu, Y. (2013). Case study of a giant debris flow in the Wenjia Gully, Sichuan Province,
664 China, *Natural Hazards*, 65, 835-849. <https://doi.org/10.1007/s11069-012-0395-y>, 2013.

665 Zanchetta, G., Sulpizio, R., Pareschi, M. T., Leoni, F. M., and Santacroce, R.: Characteristics of May 5-6,
666 1998 volcanoclastic debris flows in the Sarno area (Campania, southern Italy): relationships to structural
667 damage and hazard zonation, *Journal of volcanology and geothermal research*, 133(1-4), 377-393,
668 [https://doi.org/10.1016/S0377-0273\(03\)00409-8](https://doi.org/10.1016/S0377-0273(03)00409-8), 2004.

669 Zhang, S., Zhang, L., Li, X., and Xu, Q.: Physical vulnerability models for assessing building damage by
670 debris flows, *Engineering Geology*, 247, 145-158 <https://doi.org/10.1016/j.enggeo.2018.10.017>, 2018.

671 O'BRIEN J. 1986. Physical processes, rheology and modeling of mudflows. Doctor of Philosophy
672 dissertation. Colorado State University.